Supporting Information

for

Microfluidic Thermally Activated Materials for Rapid Control of Macroscopic Compliance

By *Aditya Balasubramanian, Mike Standish* and *Christopher J Bettinger**

Table S1. Nominal and actual dimensions of microfluidic geometries measured using SEM. Volumetric flow rates of thermal perfusate are also included.

Nominal dimensions				Actual dimensions			
Sample geometry	Channel width, *W* (μm)	Channel height, *H* (μm)	Interchannel distance, *d* (μm)	Channel width, *W* (μm)	Channel height, *H* (μm)	Interchannel distance, *d* (μm)	Flow rate, *Q* (ml s^{-1})
TS500	500	500	500	371 ± 46	443 ± 34	710 ± 18	1.17 ± 0.04
TS1000	500	500	1000	526 ± 16	492 ± 20	1040 ± 43	0.971 ± 0.043
TS1500	500	500	1500	553 ± 43	501 ± 13	1540 ± 71	0.827 ± 0.012

Calculating predicted storage modulus of MicroLat structures:
The modulus of open cell foams can be related to the relative density of the foams as follows:

$$\frac{E}{E_s} = C\left(\frac{\rho}{\rho_s}\right)^2 \qquad \text{Eqn.1}$$

E is the modulus of the foam, E_s is the modulus of the solid cell wall material, $\frac{\rho}{\rho_s}$ is the relative density of the foam and *C* is a constant. For MicroLat structures, $\frac{\rho}{\rho_s}$ = 0.485 and *C* ~ 1 is used to calculate the predicted modulus.[1] The predicted and measured storage moduli of MicroLat structures are given in Table S2.

Table S2. Storage modulus of MicroLat structures (experimental and predicted) and bulk ATPP structures at *T* = 30 ^{o}C and *T* = 80 ^{o}C.

Sample geometry	Storage modulus, *E′ (T = 30 ^{o}C)* (MPa)	Storage modulus, *E′ (T = 80 ^{o}C)* (MPa)
Bulk ATPP	688 ± 73.8	38.1 ± 1.39
MicroLat (Calculated)	162	6.59
MicroLat (Measured)	285 ± 45.8	22.1 ± 4.13

Table S3. Physical properties of ATPP used in the fabrication of microfluidic thermally activated materials.[2]

Material property	Range of values
Tensile strength (MPa)	50-65
Elongation at break (%)	10-25
Modulus of elasticity (MPa)	2000-3000
Flexural strength (MPa)	75-110
Flexural modulus (MPa)	2200-3200
HDT at 0.4 MPa (^{o}C)	45-50
HDT at 1.82 MPa (^{o}C)	45-50
Izod notched Impact (J m^{-1})	20-30
Glass transition temperature (^{o}C)	1.1-1.5
Water absorption (%)	52-54
Shore Hardness (Scale D)	83-86
Rockwell Hardness (Scale M)	73-76
Polymerized density (g m^{-3})	1.17-1.18
Typical accuracy (μm)	20-85

Table S4. Nominal sample dimensions of microfluidic geometries.

Sample geometry	Sample width, *w* (mm)	Sample height, *h* (mm)	Sample length, *l* (mm)
TS500	9.0	1.0	16
TS1000	9.0	1.5	16
TS1500	8.0	2.0	16
MicroLat	9.3	2.1	16

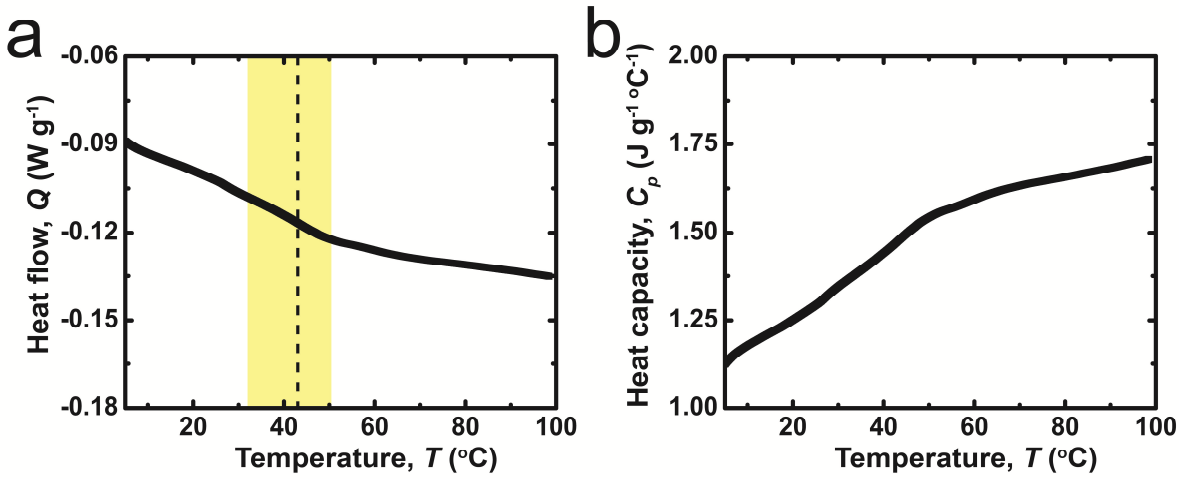

Figure S1. a) DSC thermograms of ATPP indicating the glass transition region. b) Temperature dependence of heat capacity C_p of ATPP from 10 ^{o}C to 100 ^{o}C.

Calculating anisotropic thermal conductivities from DSC plots:

DSC thermographs generated during thermal conductivity measurements of ATPP measured along axes (a) transverse and (b) parallel to the characteristic print direction of the samples are plotted in Figure S2. The slope of the linear part of the plot corresponds to the total thermal resistance *R* of the system ($\text{slope} = \frac{2}{R}$). *R* can be expressed as follows:

$$R = R_1 + R_2 + R_{ATPP} \qquad \text{Eqn.2}$$

R_1 is the thermal contact resistance between ATPP and the furnace, R_2 is the thermal contact resistance between ATPP and Indium and R_{ATPP} is the thermal resistance of the sample. R_{ATPP} can be expressed as follows:

$$R_{ATPP} = \frac{L_{ATPP}}{A_{ATPP}\, K_{ATPP}} \qquad \text{Eqn.3}$$

L_{ATPP}, A_{ATPP} and K_{ATPP} are the height, area and thermal conductivity of ATPP samples respectively. By repeating experiments with samples having constant cross-sectional area and varying heights, the thermal conductivity of ATPP was calculated (Figure 3).[3]

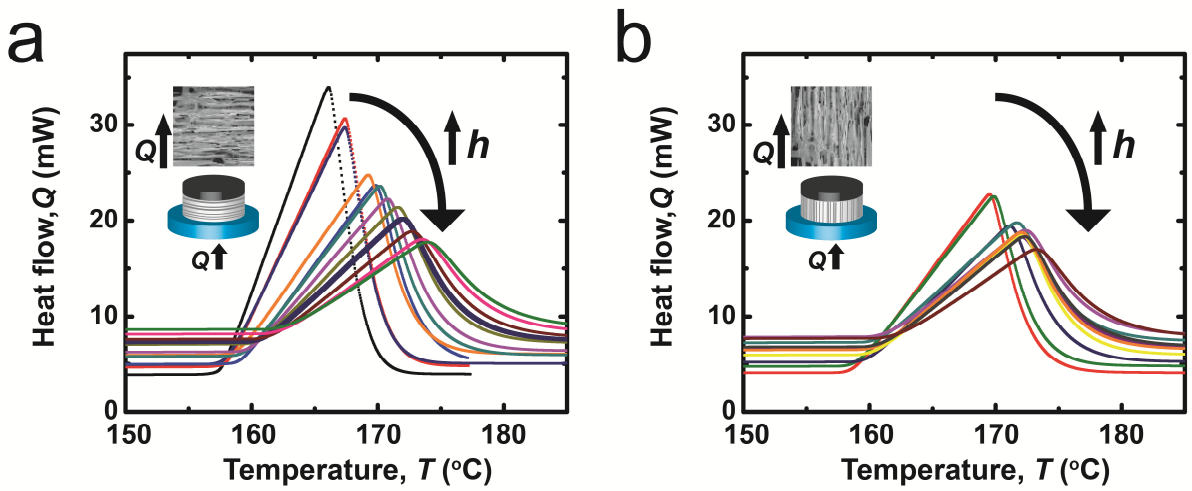

Figure S2. DSC thermograms generated during thermal conductivity measurements of ATPP. Anisotropic thermal conductivities were measured along axes (a) transverse and (b) parallel to the characteristic print direction of the samples.

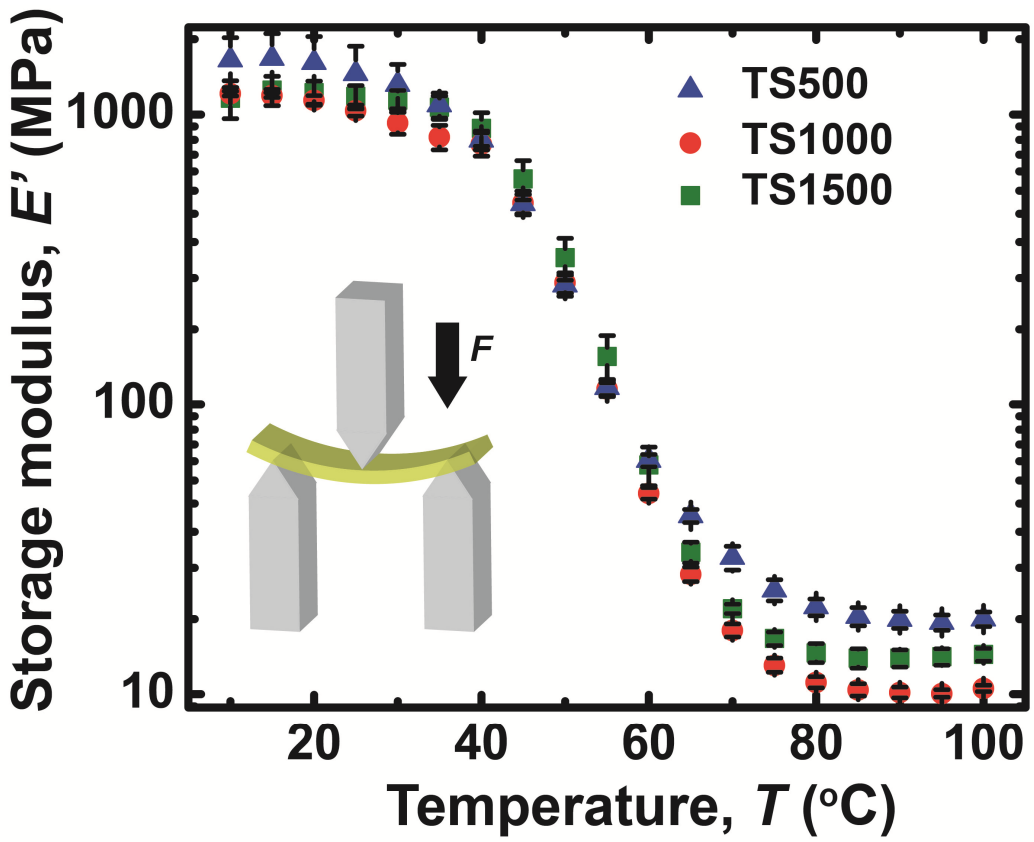

Figure S3. Thermomechanical properties of microfluidic test structures composed of ATPP measured from 10 to 100 °C.

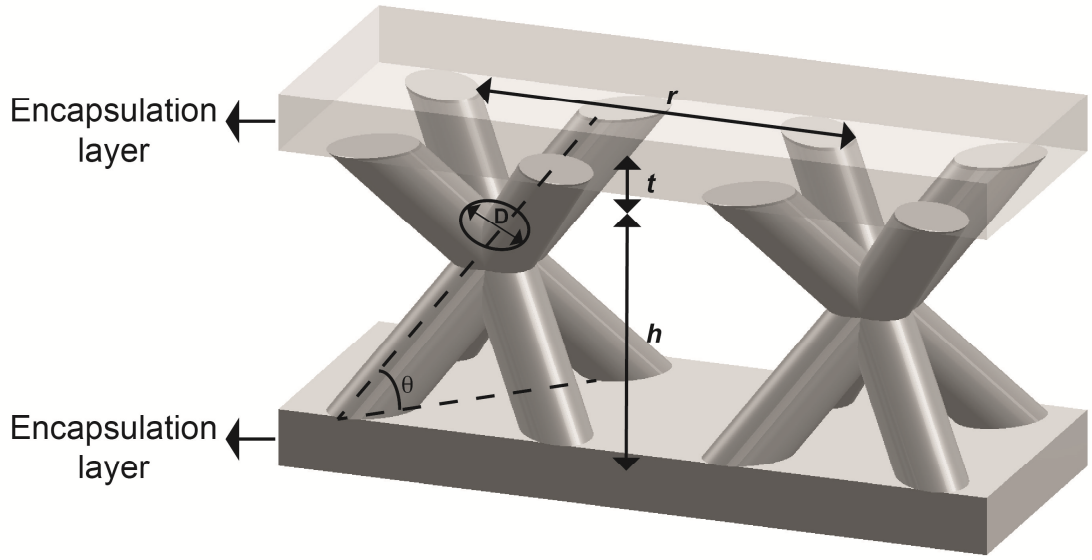

Figure S4. Schematic of MicroLat repeat unit indicating nominal dimensions with structure diameter D = 366 µm, structure angle θ = 45°, structure height h = 1500 µm, encapsulation layer thickness t = 300 µm and inter-structure distance r = 2121 µm.

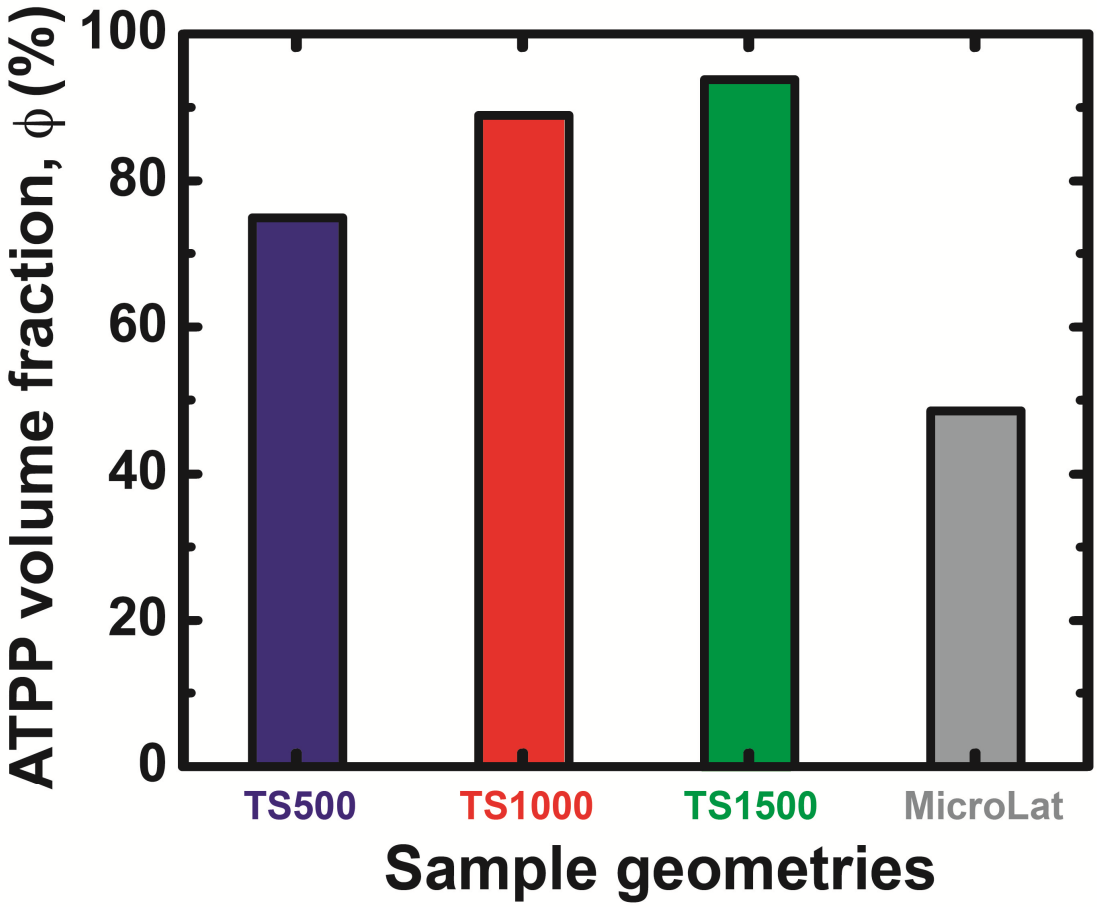

Figure S5. Comparison of ATPP volume fractions in microfluidic and MicroLat geometries. MicroLat geometries have minimal ATPP volume fraction and thus have maximal free volume for fluid flow.

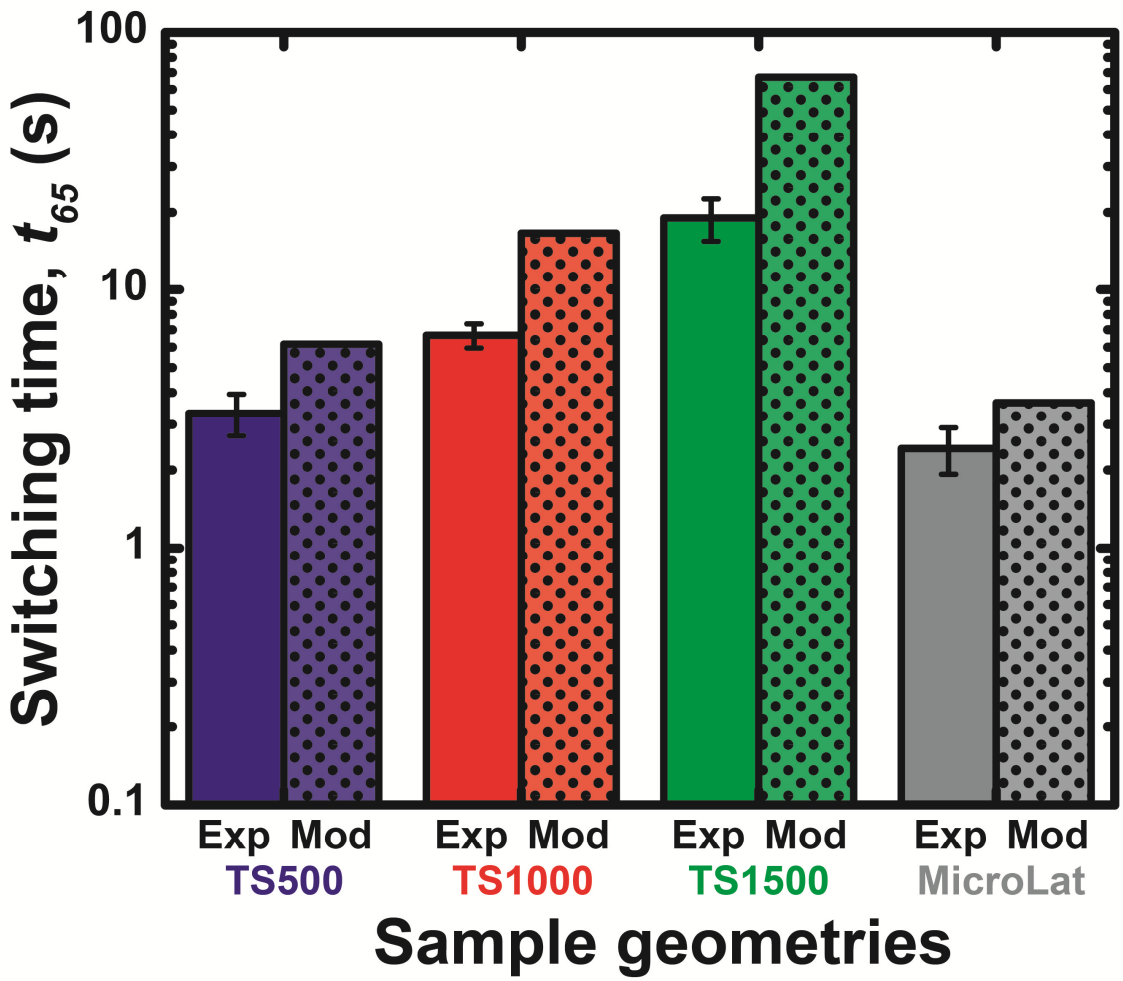

Figure S6. Comparison of the experimental and modeled t_{65} values for the microfluidic and MicroLat geometries. The disparity between predicted (via FEM) and experimental values of t_{65} increases as the channel spacing increases. Furthermore, predicted values of t_{65} are consistently higher compared to experimental values. These trends emerge due to the presence of defects. The impact of structural defects from 3D printing on the accuracy of the model increases as the channel spacing increases.

Calculating predicted temperature profiles of microfluidic and MicroLat thermally activated materials:
FEM models for discrete time points were generated using the 2D heat transfer module in COMSOL Multiphysics Version 4.2.0.150 (Figure S7**)**. Model parameters are summarized in Table S5.

ATPP material constants:
Anisotropic thermal conductivity (K_{yy} = 0.12 W m^{-1} K^{-1}, K_{zz} = 0.93 W m^{-1} K^{-1}); Density (ρ = 1.17 g cm^{-3}); Heat capacity values calculated from a line fit of Figure S1(b)($C_p = 7.107T + 1147$ J Kg^{-1} K^{-1}).

Boundary conditions:
The cross-sectional sample geometries were constructed and surface convective cooling coefficients ranging from of H = 5 - 50 W m^{-2} K^{-1} were used in the FEM. These values represent the normal convective cooling range observed during free convection of air[4]. Convective heat transfer effects within the sample channels were negligible compared to the overall convective cooling of the water heating system.

Table S5. FEM Boundary conditions for microfluidic and MicroLat geometries.

Sample geometry	Parameters for time-dependent internal boundary temperature (T_o)			Ambient temperature, T_∞ (K)	Convective cooling coefficient, h (W m^{-2} K^{-1})
	a	*b*	*c*		
TS500	-0.06	353.1	-	297.4	45
TS1000	-0.06	353.1	-	297.9	27
TS1500	-0.06	353.1	-	298.9	27
MicroLat	359.6	81.71	582.1	302.7	50

The overall drop in temperature of the water flowing through the channels due to system cooling effects was measured and integrated with the internal boundary conditions. The time-varying internal boundary condition for the linear microfluidic array geometries was fit to the following expression.

$$T_0 = at + b \qquad \text{Eqn.4}$$

In this expression, t is the heating time (s) and a (s^{-1}) and b (K) are constants. In the MicroLat geometry, the time-varying internal boundary condition was fit to the following expression.

$$T_0 = ae^{-(\frac{t-b}{c})^2} \qquad \text{Eqn.5}$$

In this equation, a (K), b (s) and c (s) are constants. The form of this expression differs between linear microfluidic arrays and MicroLat geometries because the latter can switch more rapidly thereby overcoming systemic perturbation in transient cooling of the perfusate.

The triangulation method was assigned as free triangular to create a user-defined fine mesh. Temperature profiles for discrete time points were generated. Values of convective cooling coefficients for which the model best fit the experimental data were extracted.

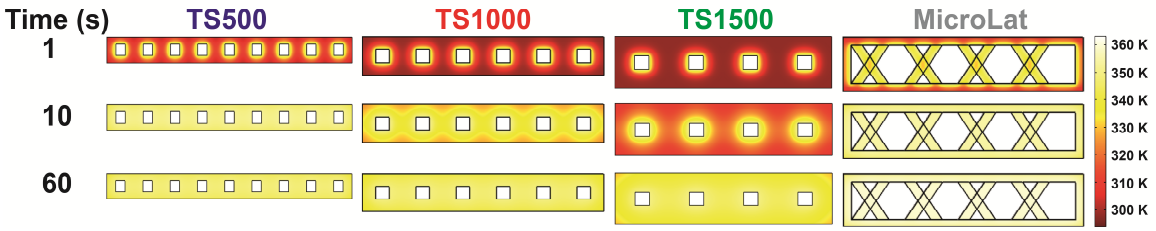

Figure S7. FEM cross-sectional profiles of microfluidic and MicroLat geometries at times *t* = 1, 10, and 60 s.

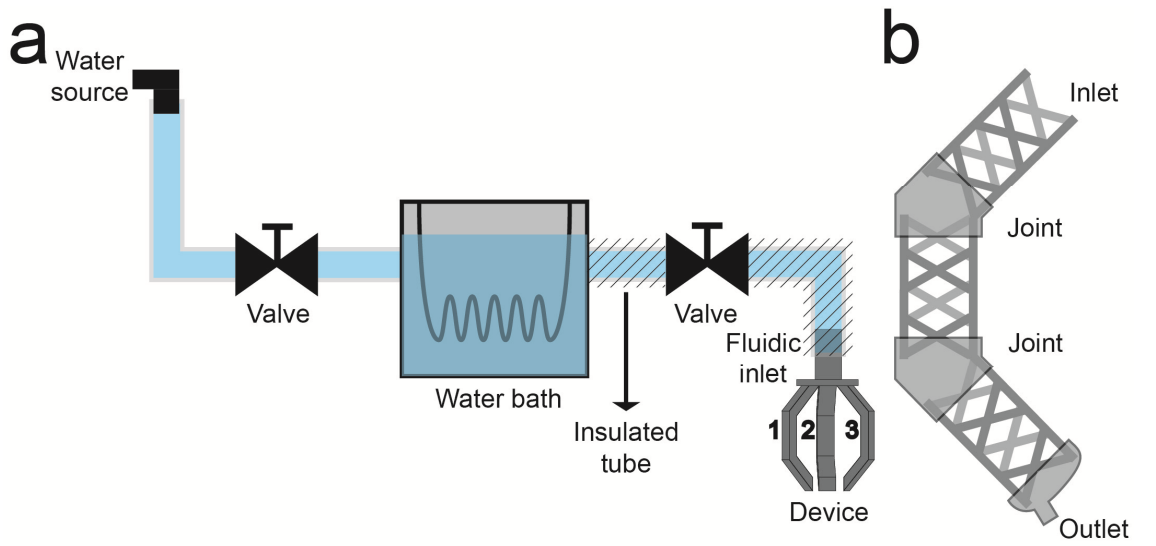

Figure S8. a) Schematic of experimental apparatus for gripper demonstration. b) Cross section of a single gripper arm indicating the internal structure, fluidic inlet and outlet, and the joints.

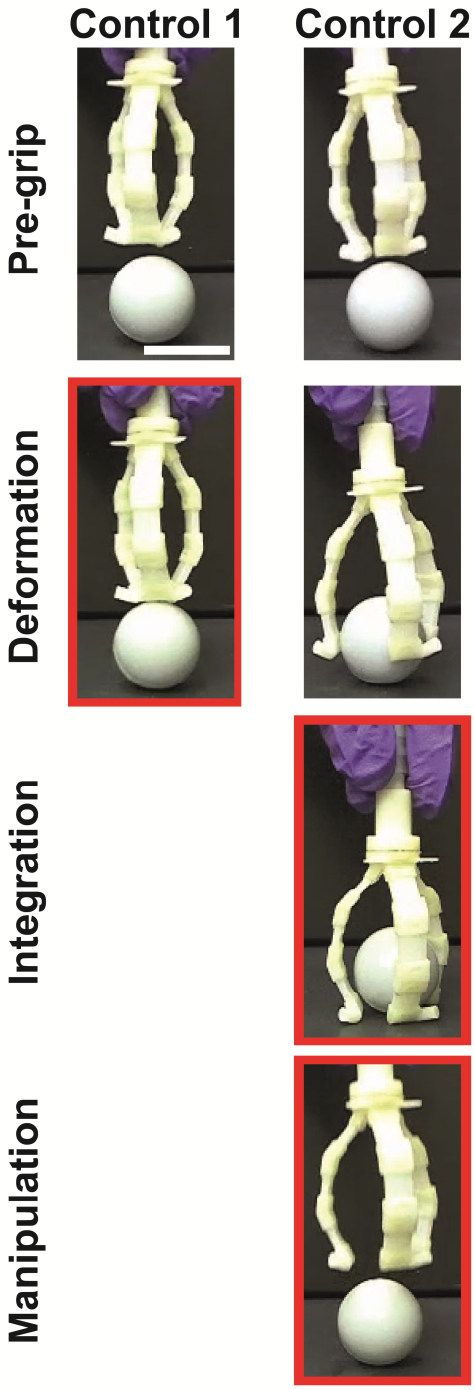

Figure S9. Actuation of materials requires coordinated thermomechanical transition of structural components. Components that are not perfused are incapable of deformation to ensconce the object of interest. Components that are not sufficiently cooled are unable to secure and support the object during the integration and manipulation stages. Scale bar indicates 2 cm.

Estimating the fluidic forces opposing the applied bending stress:

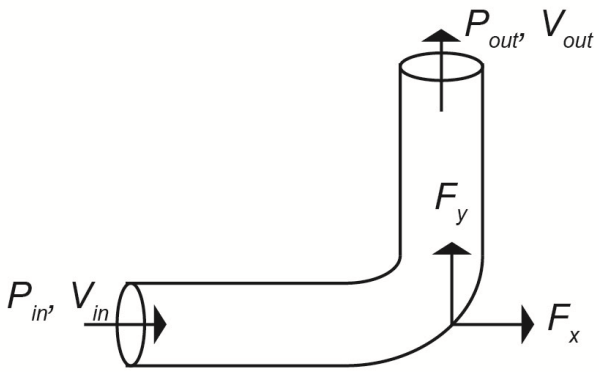

Figure S10. Schematic indicating the forces on a microfluidic channel bend.

We consider a single cylindrical microfluidic channel system of cross-sectional area (*A*) with water flowing at a rate (*Q*) equal to the value represented in the systems discussed in the manuscript. The pressure of the water is assumed to be 10 kPa. Assuming the system bends by $\theta = 90^{o}$, the force of water on the bend would oppose the applied bending. In order to determine this force, the forces on the bend along the *x* (F_x) and *y* (F_y) axis is calculated (Figure S10) using the following equations.

$$F_x = \rho Q[V_{x\,in} - V_{x\,out}] + P_{x\,in}A + P_{x\,out}A \qquad \text{Eqn.6}$$

$$F_y = \rho Q[V_{y\,in} - V_{y\,out}] + P_{y\,in}A + P_{y\,out}A \qquad \text{Eqn.7}$$

The terms in the above equations are as follows: ρ is the density of water, $V_{i\,in}$ is the inlet water velocity in the *i* direction, $V_{i\,out}$ is the outlet water velocity in the *i* direction, $P_{i\,in}$ and $P_{i\,out}$ are the inlet and outlet pressures in the *i* direction. Using the values A = 0.25 mm^2, Q = 0.17 ml/s, $V_{x\,in} = V_{y\,out}$ = 0.68 m/s, $V_{x\,out} = V_{y\,in}$ = 0 m/s, $P_{x\,in} = P_{y\,out}$ = 10 kPa and $P_{x\,out} = P_{y\,in}$ = 0 kPa, F_x and F_y were calculated to be 3 mN and -3 mN, respectively. Thus the overall force acting on the bend is given by the following equation.

$$F = \sqrt{{F_x}^2 + {F_y}^2} \qquad \text{Eqn.8}$$

The total force acting on the bend F = 4 mN. Increasing P_{in} and Q tenfold results in F = 36 mN and 20 mN on the channel bend, respectively. For structures with *l* x *w* x *h* = 10 x 2 x 2 mm and elastic modulus E ~ 20 MPa, the force required for $\theta = 90^{o}$ deflection (F_{bend}) would be ~ 6 N. Since F < 1% F_{bend} even with the increase in flow rate and inlet pressure, the momentum effects of fluid handling within microfluidic networks do not deform the resulting microstructures.

Additional References

[1] L. J. Gibson, *Journal of Biomechanics* **2005**, *38*, 377.

[2] Physical properties of proprietary Verowhite^{TM} material as reported by Stratasys, Eden Prairie, MN, USA (http://www.stratasys.com).

[3] C. P. Camirand, *Thermochimica Acta* **2004**, *417*, 1.

[4] J. R. Welty, C.E. Wicks, R.E. Wilson, G.L.Rorrer, *Fundamentals of Momentum, Heat, and Mass Transfer, 5th Edition*, 2008*;* pp. 208.